Nuclear shape evolution based on microscopic level densities

D. E. Ward,[1] B. G. Carlsson,[1] T. Døssing,[2] P. Möller,[3] J. Randrup,[4] and S. Åberg[1]

[1]*Mathematical Physics, Lund University, Box 118, S-221 00 Lund, Sweden*
[2]*Niels Bohr Institute, DK-2100 Copenhagen Ø, Denmark*
[3]*Theoretical Division, Los Alamos National Laboratory, Los Alamos, New Mexico 87545, USA*
[4]*Nuclear Science Division, Lawrence Berkeley National Laboratory, Berkeley, California 94720, USA*

By combining microscopically calculated level densities with the Metropolis walk method, we develop a consistent framework for treating the energy and angular-momentum dependence of the nuclear shape evolution in the fission process. For each nucleus under consideration, the level density is calculated microscopically for each of more than five million shapes with a recently developed combinatorial method. The method employs the same single-particle levels as those used for the extraction of the pairing and shell contributions to the macroscopic-microscopic potential-energy surface. Containing no new parameters, the treatment is suitable for elucidating the energy dependence of the dynamics of warm nuclei on pairing and shell effects. It is illustrated for the fission fragment mass distribution for several uranium and plutonium isotopes of particular interest.

I. INTRODUCTION

The highly dissipative character of collective nuclear dynamics renders the evolution of the nuclear shape akin to Brownian motion. As a result, it has proven possible to describe the fission process as a Metropolis walk on the associated multidimensional potential-energy surface [1]. This calculationally simple method has yielded remarkably good fission-fragment mass distributions [2]. Though merely a rough approximation to the underlying Langevin-type transport description of the nuclear shape dynamics, the Metropolis treatment has proven to be quantitatively useful and, because tabulations of suitable potential-energy surfaces exist for essentially all nuclei of potential interest [3], the method has made it possible to predict fission fragment mass distributions for poorly explored regions of the nuclear chart [4,5].

Using χ to characterize the multidimensional shape, we may denote the potential-energy surface by $U(\chi)$. It is important to recognize that $U(\chi)$ represents the shape dependence of the potential energy of *cold* nuclei, i.e., $U(\chi)$ is the energy of the lowest possible configuration compatible with the shape χ. However, in processes such as induced fission the nuclear system is generally *warm*, i.e., the *local* excitation energy, $E^*(\chi) \equiv E - U(\chi) > 0$ (where E denotes the given total energy), is typically several MeV. Therefore it is necessary to develop a treatment that takes proper account of the local excitation. In particular, it is essential to understand the energy dependence of the pairing and shell effects which play major roles in fission dynamics and have a decisive influence on the appearance of the fission-fragment distribution. Qualitatively speaking, as the nuclear excitation is increased these microscopic corrections tend to subside and the resulting effective potential gradually acquires a purely macroscopic form; accordingly, for actinides, the fragment mass distribution evolves from being asymmetric to being symmetric.

This phenomenon was recently addressed in a preliminary manner by using an *ad hoc* energy-dependent suppression function to reduce the microscopic term in the potential energy [2]. While apparently quite successful, such an approach

is not satisfactory from a theoretical perspective because it does not properly take into account the considerable structure of the nuclear level density and its dependence on the nuclear shape. In particular, the approach does not take into account the different energy scales for the decrease of the pairing and shell corrections. There is therefore a need for addressing the problem in a more fundamental manner. Towards this end, the present paper presents a formally well-founded approach to the energy dependence of the fission shape evolution.

We employ a recently developed combinatorial method [6] for generating the nuclear level density from the single-particle levels in the mean field associated with the given deformed system. In that work [6], level densities were calculated and compared to data at equilibrium shapes of the excited nucleus. We here extend the treatment to arbitrary shapes and make applications to the shape evolution in nuclear fission, which generally involves shapes that are not situated at stationary points of the potential-energy surface. Furthermore, we include the total angular momentum which is conserved. Because the single-particle levels in the level-density calculation are the same as those used for the calculation of the microscopic contributions to the potential-energy surface, the approach is consistent and no new parameters are required. This microscopically based shape-dependent level density, $\rho(E, I; \chi)$, then provides, in a well-defined manner and at arbitrary energy E and angular momentum I, the statistical weights required for the transport treatment of the nuclear shape dynamics. In particular, using the Metropolis treatment [1], we study the energy dependence of fission fragment mass distributions.

In addition to the physics insight gained, the present development is expected to be useful as a means for providing energy-dependent mass yields for fission event generators, such as FREYA [7], FIFRELIN [8], or CGMF [9], especially for cases where no experimental information is available (or cannot be obtained in practice).

In Sec. II we briefly review the combinatorial method and discuss its adaptation to the description of the density of states for shapes relevant to fission. Section III summarizes the Metropolis method of the shape evolution and describes

how the required statistical weights are obtained on the basis of the calculated level densities. The resulting refined treatment is then applied to a number of instructive cases in Sec. IV, and our concluding remarks are given in Sec. V.

II. LEVEL DENSITIES AT HIGH EXCITATION

In this section we discuss the adaptation of the combinatorial method for calculating level densities to fission dynamics. Relative to the original work [6], the description of fission requires a large number of relatively complex shapes that are typically reflection asymmetric, and the internal excitation energies may grow to several tens of MeV as scission is approached.

First, in Sec. II A, the combinatorial method is briefly reviewed, and the effects from pairing and shell structure are examined in Sec. II B. Then, in Sec. II C, the acquired insight is used to extrapolate the microscopic level density to higher excitation energies.

A. Combinatorial level-density method

In Ref. [6] a method was developed for microscopic calculations of level densities for deformed nuclei and we shall adapt it to the fission process. For a specified shape χ, the single-particle levels for protons and neutrons needed for the combinatorial calculation of the level density are obtained by solving the Schrödinger equation in the associated folded-Yukawa potential. These levels were already used in Ref. [3] to calculate the microscopic shell and pairing energies in the construction of the potential-energy surfaces. The corresponding local many-body vacuum state $|0; \chi\rangle$ has N neutrons and Z protons filling the lowest single-particle states, and the uncorrelated excited states consist of all multiple particle-hole excitations,

$$|i; \chi\rangle = \prod_{n \geqslant 1} a^{\dagger}_{\nu_n^{(i)}} a_{\mu_n^{(i)}} |0; \chi\rangle. \qquad (1)$$

For each many-body state $|i; \chi\rangle$, blocked BCS calculations for neutrons and protons separately provide the state-dependent pairing gaps, $\Delta_i^n(\chi)$ and $\Delta_i^p(\chi)$, respectively, and the energy of the correlated intrinsic many-body state, $E_i(\chi) = E_i^n(\chi) + E_i^p(\chi)$.

All nuclear shapes considered in the present study have axial symmetry (around the z axis), so the angular momentum component along the symmetry axis, K_i, is a good quantum number for the state $|i; \chi\rangle$. The value of $K_i(\chi)$ is given in terms of the individual particles and holes in the intrinsic state (1). Because the shapes relevant for the present fission study are well deformed, we assume that a rotational band can be built on each intrinsic configuration.

For a given value of K, the total angular momentum I may take on the following values,

$$I = K, (K + 1), (K + 2), \dots . \qquad (2)$$

and the corresponding rotational energies of the band members are

$$E_i^{\text{rot}}(I; \chi) = \frac{I(I + 1) - K_i(\chi)^2}{2\mathcal{J}_{\perp}(\chi, \Delta_i^n(\chi), \Delta_i^p(\chi))}. \qquad (3)$$

The moment of inertia $\mathcal{J}_{\perp}$ is approximated by the moment of inertia of a rigid body with the shape χ, modified by the calculated pairing gaps for the state [10]. The total energy of a state is then given by

$$E_i(I, \chi) = E_i^n(\chi) + E_i^p(\chi) + E_i^{\text{rot}}(I; \chi). \qquad (4)$$

For each shape χ, the resulting states are binned according to their energy E_i and their total angular momentum I; the values at arbitrary energies are then obtained by linear interpolation. The bin width is usually taken as $\Delta E = 200$ keV. For local excitation energies $E^* \gtrsim 3$ MeV, the mean level spacing is $1/\rho(E^*) \lesssim 1$ keV, and the level density is insensitive to the bin width. But at low excitation energies the discreteness of the energy levels makes this treatment less accurate. For example, due to the pairing gaps, only the local ground state exists within the lowest energy bin and the next several bins are empty. The binning effectively introduces a smearing of individual energy levels of the order of ΔE and so, in the random walk on the shape lattice, the system can access a given site if its energy lies within ΔE of any of the levels at that site. We have tested the sensitivity of our results to the bin size and found that doubling or tripling ΔE produces negligible changes in the calculated mass distributions.

B. Pairing and shell structure at high excitation

In Fig. 1 we show calculated level densities versus the backshifted excitation energy for three special shapes in the fission process of ^{236}U, all calculated for the angular momentum $I = 4\hbar$: (i) the shape of the isomeric (second) energy minimum shape, which has a large negative shell energy, (ii) the shape associated with the symmetric barrier, which has a large positive shell energy, and (iii) a shape in between having a rather small shell energy. For each of these
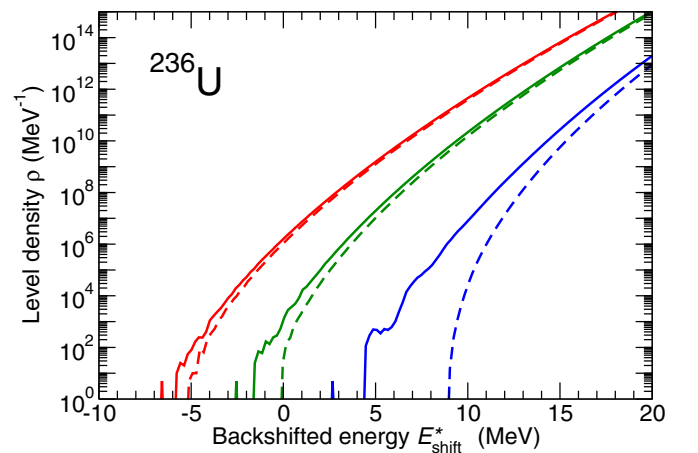

FIG. 1. The microscopic level density, $\rho(E^*)$, calculated for ^{236}U at angular momentum $I = 4\hbar$ and plotted versus the backshifted energy, $E_{\text{shift}}^* = E^* + E_{\text{sh}} + E_{\text{pc}}$, shown for three selected shapes: (i) the second minimum (red/left) ($E_{\text{sh}} = -5.4$ MeV, $E_{\text{pc}} = -1.5$ MeV), (ii) the outer symmetric fission barrier (blue/right) ($E_{\text{sh}} = +8.7$ MeV, $E_{\text{pc}} = -6.1$ MeV), and (iii) a shape in between (green/middle) ($E_{\text{sh}} = -0.3$ MeV, $E_{\text{pc}} = -2.5$ MeV), either with (solid) or without (dashed) pairing.

shapes, the level density is calculated both without and with pairing. The resulting level densities are plotted against the backshifted energy given by the actual excitation plus the shell and pairing energies of the local ground state, $E^*_{\text{shift}}(\chi) = E^*(\chi) + E_{\text{sh}}(\chi) + E_{\text{pc}}(\chi)$. The pairing condensation energy, E_{pc}, is defined as the difference between the BCS ground-state energy and the energy of the unpaired ground state. For the calculations without pairing we have $E_{\text{pc}} = 0$, so for the intermediate case having $E_{\text{sh}} \approx 0$ we have $E^*_{\text{shift}} \approx E^*$ and the backshifted excitation energy is approximately zero for the local ground state. For this case the level density is close to that of a Fermi gas already at quite low excitation energies. By comparing the level density versus E^*_{shift} for the different cases, we can elucidate how the level density develops with excitation energy due to the gradual decrease of the pairing correlations and the shell effects.

At the second minimum, the gaps in the single-particle spectra for neutrons and protons provide the special stability of this shape region, quantitatively expressed by a considerable negative shell correction energy, $E_{\text{sh}} = -5.4$ MeV. On the other hand, the same gaps render it costly in energy to make particle-hole excitations, resulting in a slow increase of the level density when the nucleus is excited. The opposite situation is encountered at the symmetric barrier, where a high density of single-particle states around the Fermi energy results in a large positive shell correction energy $E_{\text{sh}} = 8.7$ MeV, while at the same time delivering particle-hole states at a low cost in energy, providing a rapid increase of the level density with local excitation energy.

These opposite effects of the shell structure on the lowest energy and on the level density cause the no-pairing results (dashed curves on Fig. 1) to converge towards the level density with zero shell energy, illustrating the suppression of shell energy with increasing excitation energy, as discussed in Refs. [11–13].

Including pairing (solid curves in Fig. 1), one sees that the dense single-particle spectra for the symmetric-barrier shape produces a strong effect, yielding a condensate energy of $E_{\text{pc}} = -6.1$ MeV. Along with the condensate energy comes a gap in the spectrum between the ground state and the excited states, and eventually a weakening of the pair correlations with increasing excitation energy. The ground state lies at $E^*_{\text{shift}} = 2.6$ MeV, two-quasiparticle states dominate at around 4–6 MeV, and four-quasiparticle states are dominant for 6–8 MeV. This structure can be recognized as bumps in the resulting level density shown Fig. 1. The spectrum grows ever more regular with increasing excitation energy and the level density becomes correspondingly smooth.

As more and more particle-hole excitations are added, the pairing correlations weaken, and the curves in Fig. 1 with pairing included (solid) converge towards the respective results without pairing (dashed). The second-minimum shape with its negative shell energy has a smaller pairing energy ($E_{\text{pc}} = -1.5$ MeV), and the level-density curve with pairing included quickly approaches the no-pairing curve as the energy is increased. We can conclude that at some excitation energy (that depends on the pairing condensate energy of the ground state) the effects of pairing on the level density are negligible.

Both effects on the level density, coming from shell structure and from pairing correlations, subside smoothly as the excitation energy increases. Two different energy scales are involved, with the pairing disappearing at a lower excitation energy than the shell structure. The present study of fission shape evolution considers a large number ($> 5 \times 10^6$) of nuclear shapes and, consequently, a large variety of shell and pairing energies appear. It is therefore of importance to employ a level density that accounts for the changes in shell and pairing effects when the shape is varied. This can be ensured by employing a microscopic calculation of the level density up to sufficiently high excitation energies for all shapes considered. However, the microscopic calculation of the level density of ^{236}U up to excitations of 25 MeV for a single shape takes roughly one week of CPU time. Performing such calculations for the more than five million shapes considered is thus presently impractical. Therefore, to reduce the computation times, we introduce below an extrapolation scheme that takes account of the changes in pairing and shell effects with excitation energy for each shape.

C. Extrapolation of level densities

As illustrated by the examples displayed in Fig. 1, most of the specific structure of the level density appears below 6 MeV of local excitation energy, such as spectral gaps or nonmonotonic behavior of the level density (or its derivative). Therefore, for all shapes χ, the calculated combinatorial level density is employed up to a local excitation $E_{\text{m}} \approx 6$ MeV and then smoothly continued upwards by an analytical expression. In this way, important structures in the level density are maintained, while the numerical calculations are kept to a manageable level (about 3 CPU seconds per shape). For each particular shape χ, the extrapolation makes use of its specific shell and pairing energies, $E_{\text{sh}}(\chi)$ and $E_{\text{pc}}(\chi)$. Their influence diminishes with increasing energy, and the level density approaches the analytical expression for a Fermi gas.

We employ the following simple analytical Fermi-gas expression [14], which is suitable for deformed nuclei with a fixed small angular momentum:

$$\rho(N, Z, E^*(\chi), I) \sim E_{\text{intr}}^{-3/2} \exp(2\sqrt{a_0 E_{\text{intr}}}), \qquad (5)$$

where $E_{\text{intr}} = E^*(\chi) - I(I + 1)\hbar^2/2\mathcal{J}_\perp(\chi)$ is the approximate intrinsic energy of a state in a rotating nucleus with angular momentum I and moment of inertia $\mathcal{J}_\perp(\chi)$. The single-particle level-density parameter is

$$a_0 = A/e_0 \qquad (6)$$

for mass number A, where e_0 is a constant determined below. Accounting for the different energy scales of shell effects and pairing effects, we introduce a backshifted intrinsic excitation energy $\tilde{E}_{\text{intr}}$, which is similar to the effective excitation E^*_{eff} of Ref. [2] (see the Appendix) and can be considered as a generalization of the prescription originally employed by Ignatyuk *et al.* [13],

$$
\begin{aligned}
\tilde{E}_{\text{intr}}(\chi) = E_{\text{intr}}(\chi) &+ (1 - e^{-E_{\text{intr}}(\chi)/E_{\text{d,sh}}})E_{\text{sh}} \\
&+ (1 - e^{-E_{\text{intr}}(\chi)/E_{\text{d,pc}}})E_{\text{pc}},
\end{aligned} \qquad (7)
$$

where E_{sh} is the shell-correction energy and E_{pc} is the pairing condensation energy. Both quantities are specific to each considered shape χ. $E_{\text{d,sh}}$ is a parameter that sets the energy scale for the melting of shell structure and $E_{\text{d,pc}}$ is the corresponding energy scale for the melting of pairing correlations. The form of the pairing shift, the third term in Eq. (7), is chosen for simplicity. It approximately includes the rapid decrease of the pairing correlations seen when comparing the level densities obtained in microscopic calculations with and without pairing; see Fig. 1. The low-energy irregularities are accounted for by the microscopic level density. By fitting the analytic expression for a number of typical shapes (see below), optimal values of $E_{\text{d,sh}}$ and $E_{\text{d,pc}}$ are determined and then applied for all shapes. The full backshift, $\tilde{E}_{\text{intr}} = E_{\text{intr}} + E_{\text{sh}} + E_{\text{pc}}$ (used as the abscissa in Fig. 1), emerges when E_{intr} is much larger than both damping scales.

The extrapolation of the level density is then given by the following analytical expression,

$$\rho(N, Z, E^*(\chi), I) = C(\chi)\tilde{E}_{\text{intr}}^{-3/2} \exp(2\sqrt{a_0 \tilde{E}_{\text{intr}}}), \quad (8)$$

where the normalization constant C is determined by continuity with the corresponding microscopic value at the matching energy $E^*(\chi) = E_{\text{m}}$, for which we use $E_{\text{m}} = 5.9$ MeV for all shapes (see below).

The three parameters introduced above, e_0, $E_{\text{d,sh}}$, $E_{\text{d,pc}}$, are determined by a nonlinear least-squares fit of the logarithm of the extrapolated values to the corresponding microscopically calculated level densities for ^{236}U. The microscopic level density is evaluated for $E^*(\chi) = 5.9, 6.1, \ldots, 20.1$ MeV, and for angular momenta $I = 0, 1 \ldots, 9$ at 15 different representative shapes between the second minimum and the outer barrier. These shapes include both symmetric and asymmetric shapes having negative as well as positive shell-correction energies.

The fit yields the optimal values $e_0 = 10.48$ MeV, $E_{\text{d,sh}} = 13.18$ MeV, and $E_{\text{d,pc}} = 4.07$ MeV. The root-mean-square error of the logarithm of the extrapolated level densities is 0.20, the largest error being a factor 1.9 occurring for angular momentum $I = 8$ at the excitation energy $E^*(\chi) = 20.1$ MeV. Figure 2 compares the extrapolated results to the microscopic calculations for three different shapes. As can be seen, the agreement is good. The extrapolation formula captures the variation in the level densities when excitation energy, shape, or angular momentum is varied.

Using the procedure described above, the microscopic level densities for all 5 009 325 physical sites in the five-dimensional (5D) shape lattice are calculated up to a local excitation energy of $E_{\text{m}} = 5.9$ MeV and then extended upwards by matching the form (8) using the optimal parameter values. As was done for the calculation of the potential-energy surfaces for the nuclei in the region considered here [3], the single-particle levels employed are those obtained for the nucleus ^{232}U.

III. SHAPE EVOLUTION

The fission shape evolution is treated by the Metropolis method presented in Ref. [1]. The treatment is based on the assumption that the nuclear shape is strongly coupled to the residual system so that its evolution is akin to Brownian
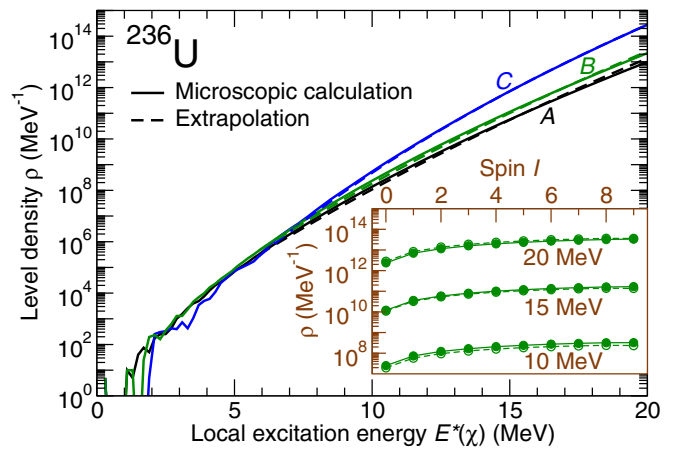

FIG. 2. Microscopic level densities (solid lines) compared to extrapolated values (dashed lines). Three different deformations for ^{236}U are considered: curve A corresponds to the second minimum, B to the asymmetric second saddle, and C to an elongated symmetric shape close to the outer barrier. Extrapolated values are shown for local excitation energies $E^*(\chi) \geqslant 6$ MeV. The inset shows the angular momentum distribution of the level density at the asymmetric saddle (B) for different excitation energies.

motion. Formally, this type of dynamics is governed by the Smoluchowski equation of motion which emerges from the general Langevin description in the highly dissipative limit.

The underlying physical picture is that the evolving system can be characterized by its shape degrees of freedom χ. The associated shape parameters are treated as classical variables which are coupled dissipatively to the remaining microscopic degrees of freedom. The resulting large-amplitude collective motion then exhibits a strongly damped diffusive evolution that can be described as a random walk on the associated multidimensional potential-energy surface $U(\chi)$. The values of the potential are available on a (five-dimensional) lattice of shapes (see below) and the Smoluchowski equation can then be approximately simulated by means of a random walk on this lattice [1].

Because the random walk must satisfy detailed balance, the following relation must hold between the rates, ν, of transition from one lattice site to another,

$$\nu(\chi \to \chi')/\nu(\chi' \to \chi) = \rho(\chi')/\rho(\chi), \quad (9)$$

where $\rho(\chi)$ is the level density at the lattice site having the shape χ. This condition can be satisfied in many ways and the Metropolis procedure [15] is merely one particularly simple possibility: A proposed shape change from χ to χ' is accepted unconditionally if $\rho(\chi') > \rho(\chi)$, whereas it it accepted only with the probability $\rho(\chi')/\rho(\chi)$ otherwise; it is readily verified that this procedure satisfies detailed balance (9).

In Ref. [1] and all subsequent applications until now, smooth Fermi-gas level-density expressions were used and the ratio between the level densities for neighboring lattice sites could therefore be approximated as

$$\rho(\chi')/\rho(\chi) \approx \exp(-\Delta U/T), \quad (10)$$

where $\Delta U = U(\chi') - U(\chi)$ is the change in the potential energy associated with the proposed shape change and $T = 1/[\partial \ln \rho(E^*)/\partial E^*]$ is the local temperature,

In the present work we wish to account for pairing correlations and shell effects. We therefore use the microscopic level densities described in Sec. II to calculate the required ratio $\rho(\chi')/\rho(\chi)$. Because those have been calculated from the same levels that were used to obtain the potential-energy surface, this provides a consistent treatment of the fission shape evolution.

The Metropolis walk is performed on a discrete lattice of more than five million shapes given in the three-quadratic-surface parametrization [16]. The five independent parameters characterizing a shape are the overall elongation of the nucleus (in terms of the reduced quadrupole moment q_2), the constriction of the central part (in terms of the neck radius c), the spheroidal deformations ε_{f1} and ε_{f2} of the two nascent fragments, and the reflection (mass) asymmetry α_g. The corresponding five lattice indices are denoted by I, J, K, L, M, respectively.

The dimensionless elongation parameter q_2 is proportional to the quadrupole moment Q_2 of the nuclear charge distribution [3],

$$q_2 = \frac{4\pi Q_2}{3 Z e R_A^2}, \tag{11}$$

where A and Z are the total mass and charge numbers of the system, respectively, and $R_A = 1.2 \, A^{1/3}$ fm is the nuclear radius.

The potential energy for the shapes in the lattice were available from previous calculations within the microscopic-macroscopic model [3],

$$U(\chi) = U_{\text{macro}}(\chi) + U_{\text{micro}}(\chi), \tag{12}$$

where $U_{\text{micro}}(\chi) = E_{\text{sh}}(\chi) + E_{\text{pc}}(\chi) - \tilde{E}_{\text{pc}}(\chi)$, where $\tilde{E}_{\text{pc}}(\chi)$ is the smooth pairing energy [17]. But, because the shell and pairing terms are needed individually for the analytical extrapolation of the microscopic level densities (see Sec. II C), those were recalculated for the present study using the same model.

A. Calculational details

At each Metropolis stage, the candidate site is selected randomly from the 242 neighboring sites in the circumscribed 5D hypercube, and the corresponding level densities are then compared in order to determine whether the step is taken or not. When the critical neck radius c_0 is reached during the walk, the value of the asymmetry coordinate α_g and the corresponding fission fragment mass and charge are registered; as in the previous studies [1,2,18], the critical neck radius used is $c_0 = 2.5$ fm. A total of 10^5 random walks are performed in each case, ensuring robust charge yield, $Y(Z_f)$, and mass yield, $Y(A_f)$.

From tests with both the previous treatment and the current refinement, it is found that the fission yields are insensitive to the starting point of the random walk, as long as it lies well inside the second barrier, as one would expect because only a single "valley" exists up to the second, isomer minimum, and

therefore equilibration occurs before the trajectory escapes over the barrier. For the cases studied in this work, this implies that one may start the random walk in the second minimum.

However, there is little advantage to merely doing that because the trajectory is likely to fall into the first minimum. Therefore the previous studies [1,2,18] employed a fictitious bias potential to reduce the probability of the random walk going further inwards when the shape is already fairly compact. To avoid the (small but existing) influence of the bias potential, we instead introduce a "wall" at the elongation corresponding to the first barrier, while the remaining potential is left unmodified. Steps that would take the random walk from a point adjacent to the wall to a point with a smaller elongation are forbidden, while all other step probabilities are calculated without modification.

To reduce the time to run a fission simulation, an upper limit on the number of steps in each random walk is used. If a random walk does not reach fission within the upper limit of steps, that trajectory is discarded altogether and not counted towards the yield. This removes trajectories stuck in hard-to-escape minima in the 5D space. A 2×10^5 step limit is used and increased if necessary to ensure that at least 70% of the tracks reach fission. By varying the step limit, we have checked that this cutoff has very little influence on the yields. For example, for ^{236}U at $E^* = 6.55$ MeV, the largest error in the mass yield is 0.0035%.

The calculations are performed for a fixed total angular momentum, I, of the compound nucleus. The influence of I on the yields is discussed in Sec. IV B. If not noted otherwise, we use $I = I_t + \frac{1}{2}$, where I_t is the known ground-state angular momentum of the isotope with one less neutron, as is most likely the case for neutron-induced fission at low energy.

We study the fission process at different excitation energies of the fissioning system. The excitation energy is measured relative the ground state of the fissioning nucleus $E_{\text{exc}} \equiv E^*(\chi_{\text{gs}})$.

IV. APPLICATIONS

In this section we apply the presented model of shape evolution to the description of fission yields of thorium, uranium, and plutonium isotopes. In Sec. IV A we discuss the structure obtained from the different trajectories in the Metropolis simulation. Consequences for the fragment yield of requiring a conserved angular momentum in the fission process are studied in Sec. IV B. In Sec. IV C calculated yields for ^{226}Th, ^{234,236}U, and ^{240}Pu are compared to experimental data and results from the previous benchmark study in Ref. [2]. The energy dependence of the fission yields is studied in Sec. IV D.

A. Metropolis shape dynamics

To obtain a general understanding of the Brownian shape evolution towards fission obtained with the Metropolis method, trajectories are studied for the case ^{236}U at $E_{\text{exc}} = 6.55$ MeV. The aggregate number of visits to different sites on the shape lattice is shown in Fig. 3, projected onto the plane of mass asymmetry α_g and elongation q_2. The solid black curve shows the mean "scission" elongation, i.e., the
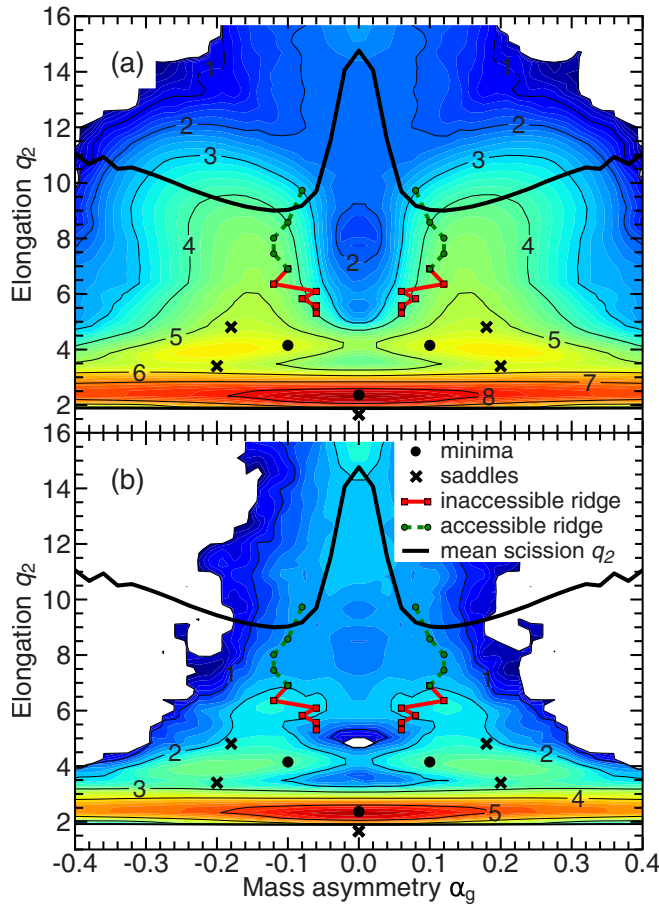
FIG. 3. $\log_{10}$(number of visits) to grid points with a given combination of asymmetry α_g and elongation q_2 for ^{236}U with $E_{\text{exc}} = 6.55$ MeV. (a) All tracks in the simulation. (b) The tracks ending in symmetric fission. Energy minima are shown as solid circles and saddle points as crosses. The solid black curve shows the mean "scission" elongation. The ridge separating symmetric from asymmetric fission paths is shown as a solid red (dark gray)/dashed green curve, where green/red indicates that the ridge is below/above the total energy, $E_{\text{exc}} = 6.55$ MeV, and thus accessible/inaccessible.

FIG. 4. Potential-energy curves for ^{236}U versus elongation, q_2. The energy path leading to asymmetric fission, starting close to the (symmetric) second minimum, is shown by a solid line. The valley leading to symmetric fission (dashed line) is separated from the asymmetric path by the ridge shown by the red (dark gray) line. The thin horizontal line indicates the excitation energy $E_{\text{exc}} = 6.55$ MeV.

average elongation, q_2, for random walks terminating with mass asymmetry α_g.

Figure 3(a) shows, in the form of a contour plot, the total number of visits to sites with a given combination of asymmetry α_g and elongation q_2, while Fig. 3(b) shows the distribution of visits for those random walks that lead to symmetric fission, $\alpha_g = 0 \pm 0.02$.

The potential-energy landscape plays a key role in the shape evolution. Its characteristic features can be determined by means of the immersion technique [3,19]. The potential-energy curve from the (symmetric) second-minimum shape via the (asymmetric) third-minimum shape leading to asymmetric fission is shown in Fig. 4. The black dots in Fig. 3 show the location of these two minima and the crosses indicate the locations of the saddle points in the potential-energy landscape.

The Metropolis walks all start in the second potential-energy minimum at $\alpha_g = 0$, $q_2 = 2.36$. From this starting point, they exhibit a diffusive track that probes the potential
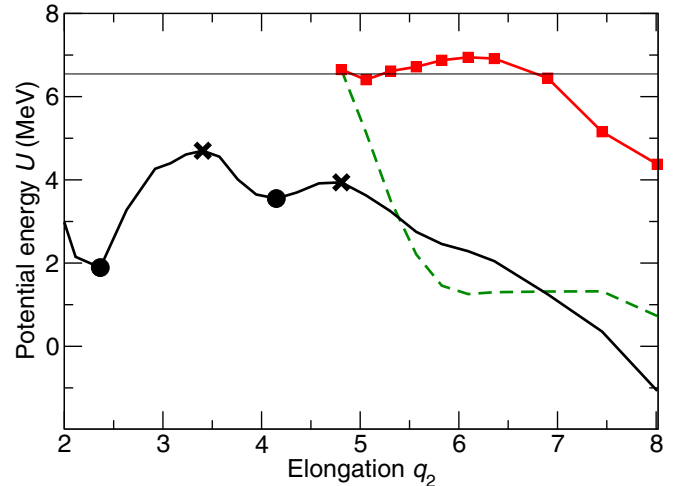
landscape at ever larger deformations, including the third minimum of potential energy located at an asymmetric shape with $\alpha_g \sim \pm 0.1$, $q_2 \sim 4$. The distribution of site visits reaches maxima in the region around the second and third minima.

Beyond the outmost saddle point(s) around $\alpha_g \sim \pm 0.2$ and $q_2 \sim 5$, the potential starts to slope steadily down towards scission; see Fig. 4. Most often, a decreasing potential is accompanied by an increase in the level density and the Metropolis walk then changes its character from being diffusive to being drift dominated and, as a result, the average number of site visits tend to become relatively constant with elongation. Concurrent with this drift in elongation, sideways diffusive steps are taken, thus providing some possibility for probing the potential with regard to changes in the fragment deformations, the neck radius, and, most importantly, the mass asymmetry. A prominent region of shapes where this kind of evolution occurs is the interval $6 < q_2 < 9$, $0.1 < \alpha_g < 0.24$ [displaying a rather uniform light green (light gray) color on Fig. 3(a)].

Turning now to symmetric shapes, $\alpha_g \simeq 0$, we note that for the considered energy, $E_{\text{exc}} = 6.55$ MeV, it is not possible to pass directly though the barrier region while keeping α_g equal to zero. Therefore, in order to reach elongated symmetric shapes, the nuclear shape must first acquire some degree of asymmetry. Figure 3(b) displays the mean number of site visits by those tracks that lead to symmetric fission. A comparison between the upper and lower parts of Fig. 3 shows that indeed the diffusion process proceeds in identical ways up to elongations of $q_2 \lesssim 5$.

But beyond that elongation, $q_2 > 5$, the potential landscape displays an asymmetric and a symmetric valley sloping towards larger elongation, separated by a ridge, see Fig. 4. The location of the ridge and its height at each elongation q_2 can be determined by application of the immersion method in
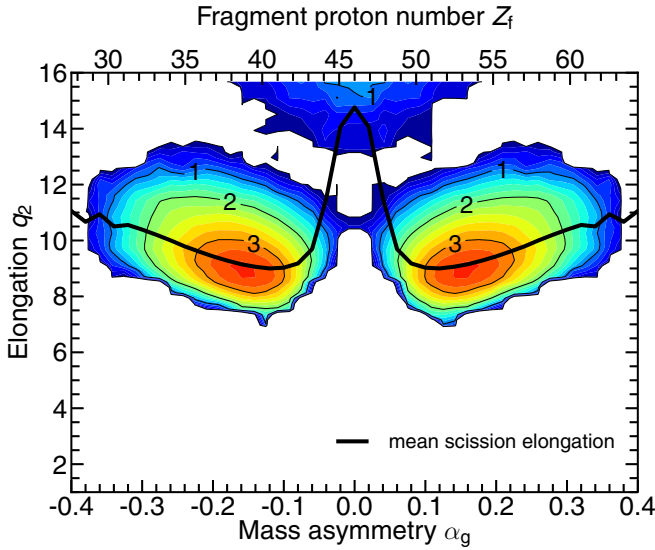
FIG. 5. Contour plot (on a logarithmic scale) of the location of the end points projected onto the (α_g, q_2) plane for fission of ^{236}U at $E_{exc} = 6.55$ MeV. Fragment proton numbers (shown on the upper axis) are obtained as $Z_f = 46(1 + \alpha_g)$.

FIG. 6. Logarithm of the ergodicity ratio, $\log_{10}(r)$, where r is given by Eq. (13), for ^{236}U with $E_{exc} = 6.55$ MeV.

the 4D shape subspace associated with that elongation. The ridge location in the (q_2, α_g) plane is displayed in Fig. 3, and the color (type of line) of the ridge line indicates if the potential energy of the ridge is above or below the total energy of the nucleus. One should here keep in mind the 5D character of the overall potential. If q_2 and α_g were the only two shape parameters, the grid points on the ridge colored red (solid dark gray) would receive no visits. With the additional shape parameters describing the fragment deformations and neck radius, it is possible to obtain a lower potential energy at the same q_2 and α_g. While these points can be visited, adding to the number of visits in Fig. 3, it is not possible for random walks in the 4D shape subspace to reach the symmetric valley if the energy is below the ridge potential energy. To reach symmetry the walk must proceed to larger elongations where the ridge between the asymmetric valley and the symmetric valley becomes lower than 6.55 MeV, which takes place around $q_2 \sim 7$; see Fig. 4.

This implies that the distribution of tracks ending up with symmetric fission, Fig. 3(b), is markedly different from the total distribution, Fig. 3(a), at elongations exceeding $q_2 \approx 7$ where the bifurcation occurs. If the ridge is surmounted the nucleus assumes a more symmetric shape and drifts towards larger elongation in the down-sloping symmetric valley. In the symmetric valley, the critical neck radius (at which the walk is terminated) typically occurs for elongations above $q_2 \approx 14$. The random walks therefore proceed to the upper central part in the figure. However, due to the end of the deformation grid at $q_2 = 15.7$ there is a local pileup as the tracks explore the shape space until the neck radius c shrinks below c_0. The extracted fragment mass distribution is practically unaffected by this artifact.

Figure 5 shows the distribution of end points for the random walks where the neck radius for the first time becomes smaller
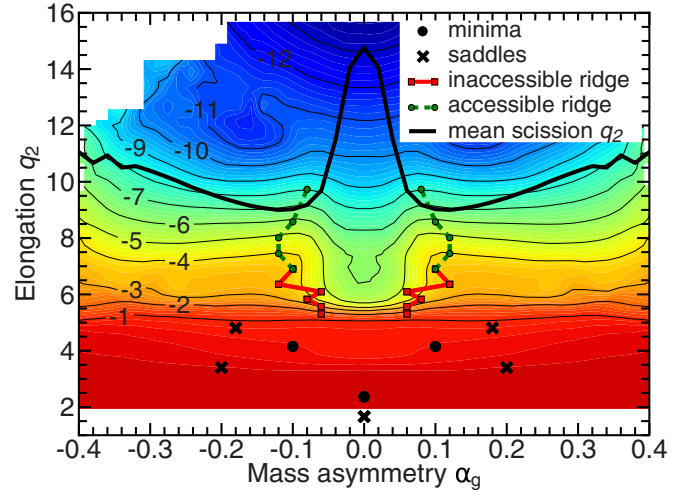
than the critical value and the mass split of the fission event is registered. The most probable end point has $\alpha_g = \pm 0.16$, $q_2 = 9.2$ [corresponding to the asymmetric peak in the charge yield in Fig. 10 (see Sec. IV D), $Z_f = 38/54$].

As noted above, symmetric fission events occur at larger elongations, shown by the local maximum in the top center of Fig. 5. This bimodal character of the end-point distribution reflects the asymmetry dependence of the shell-correction energy in the scission region: For asymmetric shapes the combined shell correction of the two prefragments encourages early neck formation, while the more symmetric configurations have a smaller shell energy.

Because the shape evolution inside the last barrier, $q_2 \lesssim 5$, is largely diffusive, one would expect a large degree of equilibration to occur in the regime of compact configurations, prior to the negotiation of the last barrier. By contrast, the subsequent drift-dominated descent towards scission proceeds relatively rapidly and is expected to have a nonequilibrium character.

A quantitative measure of the degree of local equilibration is given by the ratio between the mean number of site visits during the walks and the local level density,

$$r_{IM} = \mathcal{N} \frac{\sum_{JKL} \bar{n}_{IJKLM}}{\sum_{JKL} \rho_{IJKLM}(E_{exc})}, \qquad (13)$$

that we shall refer to as the "ergodicity ratio." Here $\bar{n}_{IJKLM}$ is the average number of visits to the shape lattice site having the indices I, J, K, L, M per walk, and $\rho_{IJKLM}(E_{exc})$ is the level density for that shape at the local excitation energy, $E^* = E_{exc} - [U_{IJKLM} - U(\chi_{gs})]$. In the sum over level densities only visited lattice sites are included. The constant $\mathcal{N}$ normalizes the ergodicity ratio to unity at the site of the second minimum.

Equilibration implies $r \approx 1$. The ergodicity ratio is shown in Fig. 6. The density of visits is relatively equilibrated up to elongation $q_2 = 5$, in agreement with the observation from Fig. 3. The equilibrated region thus ends around the outermost saddle point in the potential-energy landscape. Beyond this
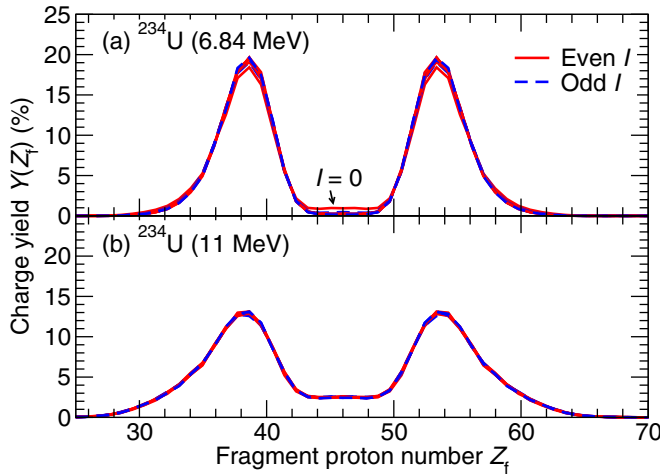
FIG. 7. Angular-momentum dependence of the yield for ^{234}U at two different excitation energies, (a) $E_{\text{exc}} = 6.84$ MeV and (b) 11 MeV. The values $I = 0, 1, \ldots, 9$ for the compound nucleus are considered. The yield curves for the different angular momenta are on top of each other, except for $I = 0$ at the thermal-neutron induced fission energy $E_{\text{exc}} = 6.84$ MeV.

elongation, the above mentioned drift towards larger deformation sets in, while the level density keeps increasing. Thus, these grid points must be visited less frequently than suggested by the accessible level density.

As points along the mean scission elongation (thick black line) have different ergodicity ratios the yield distribution is not proportional to the level density at scission shapes. This is assumed in some statistical scission models and was shown to be an oversimplification in Ref. [18].

B. Angular-momentum dependence

If there is no neutron or photon emission during the shape evolution, the angular momentum I of the fissioning system is conserved. In the current treatment, this implies that the level densities employed in the Metropolis walk should be evaluated for the given fixed angular momentum I at all the different shapes χ. For s-wave neutron-induced fission the compound system acquires one of two possible I values, namely $I_t \pm \frac{1}{2}$ where I_t is the angular momentum of the target nucleus.

To see how the fragment yields change with angular momentum, we consider fission of ^{234}U for $I = 0, 1, \ldots, 9$. The resulting charge yields are shown in Fig. 7. For the excitation energy $E_{\text{exc}} = 6.84$ MeV, the angular momentum $I = 0$ gives the smallest asymmetric peak and largest symmetric yield. The peak yield increases when I is increased for $I = 1, 2$, while the remaining angular momenta give virtually the same yields. For $E_{\text{exc}} = 11$ MeV the yields are practically independent of I.

A basic feature of the level density is the amount of rotational energy contained in the local excitation energy, proportional to $I(I + 1)$. Increasing the rotational energy decreases the intrinsic energy, effectively making the system cooler, and should thus decrease the symmetric yield. This is borne out to some degree in Fig. 7(a). This simple picture

is complicated by the fact that the level density can have a complex dependence on the angular momentum for low energies, including odd-even I staggering [20].

At sufficiently high excitation energies, the level densities show a smooth dependence on the angular momentum I, cf. the inset in Fig. 2. This implies that the ratio of level densities at adjacent lattice sites is insensitive to changes in I, and therefore the fragment yields in Fig. 7(b) show little dependence on angular momentum.

Because the yields are sensitive to the angular momentum I only at low excitation energies, the specific I value used for the compound nucleus will influence the results mainly when comparing to low-energy data. The calculations below have been carried out using $I = I_t + \frac{1}{2}$.

C. Comparison with previous calculations and experimental data

As mentioned in Sec. I, the energy dependence of fission fragment yields was previously treated using an *ad hoc* energy-dependent suppression function to describe the diminishing influence of the shell and pairing structure when E_{exc} is increased, corresponding to using an effective level density, ρ_{eff}, in Eq. (10) [2]. The suppression function was adjusted for the case of ^{234}U, where high-quality data exist for charge yields at two different energies. In the Appendix we show the correspondence between the present treatment and the earlier description with a phenomenological suppression function.

Figure 8 shows the calculated charge yields for ^{234}U, compared with yields obtained using the previous treatment with ρ_{eff} (cf. Fig. 4 in Ref. [2]) and with experimental data. The results for excitation energy $E_{\text{exc}} = 6.84$ MeV are similar, and both are in good agreement with data. For $E_{\text{exc}} = 11$ MeV, the current approach correctly reproduces the symmetric yield of around 2%. On the other hand, the yields for highly asymmetric splits are too large. The yields for $E_{\text{exc}} = 16$ MeV are quite similar in both approaches. It is noteworthy that our treatment captures most of the nontrivial energy dependence of the yields without the use of any adjustable parameters.

The charge yield for ^{226}Th at excitation energy $E_{\text{exc}} = 11.20$ MeV, and yields for ^{236}U and ^{240}Pu corresponding to ^{235}U(n_{th}, f) and ^{239}Pu(n_{th}, f) are compared to experimental data in Fig. 9.

The largest difference between the current and previous treatments occur for ^{226}Th. Using the microscopic level-density results in a lower symmetric yield, more in line with the experimental data. However, both calculations obtain the peak asymmetric yield at $Z = 33$, whereas the experimental data is peaked at $Z = 36$. (It was demonstrated in Ref. [18] that in this case the location of the asymmetric peak is quite sensitive to the deformation dependence of the Wigner term in the macroscopic energy, which is poorly understood.)

There is a very good agreement between calculation and experiment for ^{236}U in both treatments. For ^{240}Pu the asymmetric peaks are slightly lower than the data, and the symmetric valley and the far asymmetric shoulders are slightly higher, with the largest deviations occurring for the treatment using microscopic level densities.
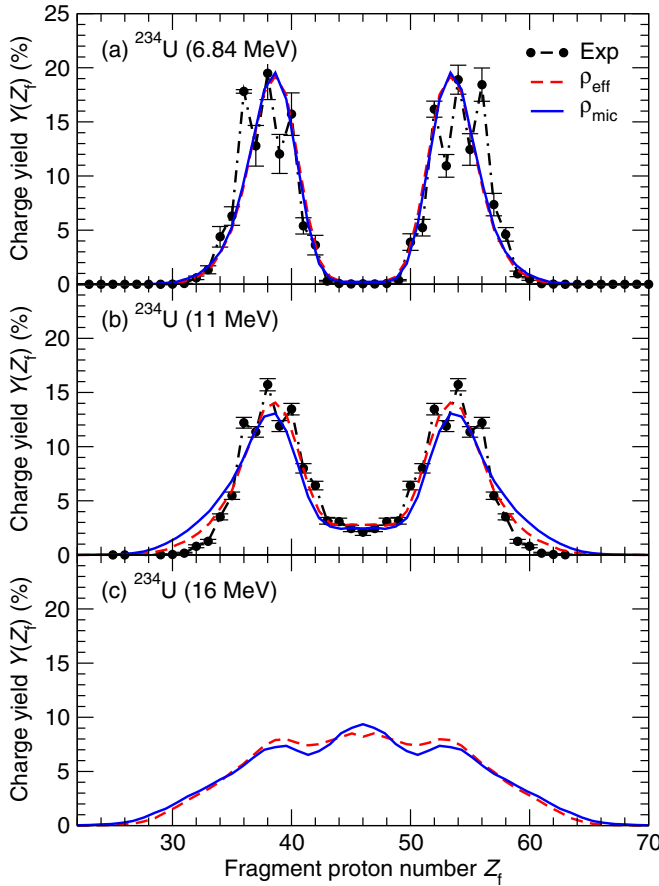
FIG. 8. Fission-fragment charge yields for ^{234}U at three different excitation energies: (a) $E_{exc} = 6.84$ MeV, (b) 11 MeV, and (c) 16 MeV. The blue solid curves have been obtained with the microscopic level densities, while the dashed red curves were calculated with the effective level density ρ_{eff} introduced in Ref. [2]. The results for $E_{exc} = 6.84$ MeV are compared to (n_{th}, f) data [21], while those for $E_{exc} = 11$ MeV are compared to (γ, f) data [22].

FIG. 9. ^{226}Th charge yields obtained using either the microscopic level density (blue solid line) or effective level-density parametrization [2] (red dashed line), compared to various experimental data: (a) ^{226}Th(γ, f) [22], (b) ^{235}U(n_{th}, f) [21], and (c) ^{239}Pu(n_{th}, f) [21]. It is not within the present scope of the models to treat the odd-even staggering seen in the data.

D. Energy dependence of yields

The transition from asymmetric to symmetric fission with increasing energy in the actinides is usually associated with the so called "melting of shell structure," with the yield gradually assuming the symmetric form characteristic of the macroscopic limit. This feature should automatically appear when the microscopic level densities are used, as discussed in Sec. II B.

Figure 10 shows the calculated charge yields from fission of ^{236}U at different excitation energies. As the energy is increased, the shape diffusion process can more directly enter the symmetric valley, both because it can surmount the ridge already at smaller elongations and because of the gradual attenuation of the microscopic effects in the level density. As a result, there is a marked increase in the symmetric component of the mass distribution as E_{exc} is increased from 6.55 to 11.55 MeV. At still higher energies the effects of pairing and shell structure are strongly suppressed, as illustrated in Fig. 1 and applied in the accurate extrapolation of the level density, Eq. (8). Consequently, the level density at high energy
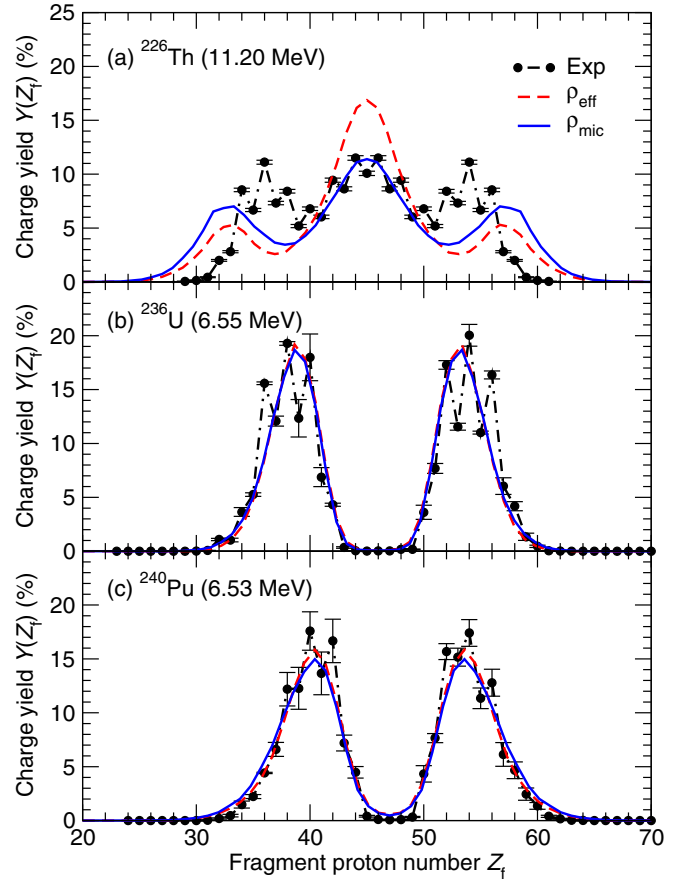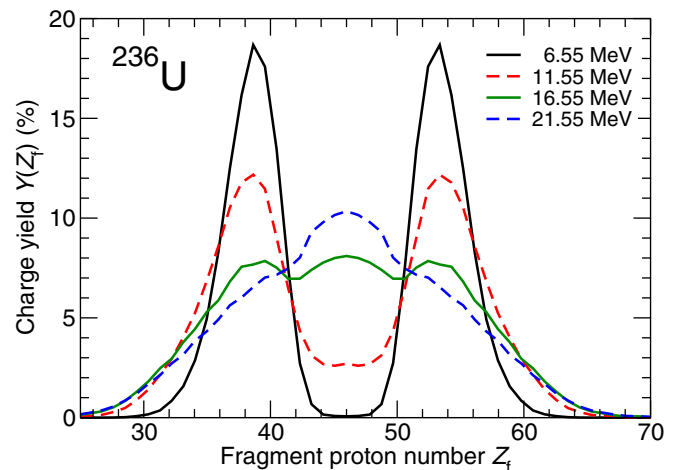

FIG. 10. Calculated charge yields for fission of the nucleus ^{236}U at four values of the excitation energy: from $E_{exc} = 6.55$ MeV ($= S_n$, the neutron separation energy) up to 21.55 MeV in steps of 5 MeV.
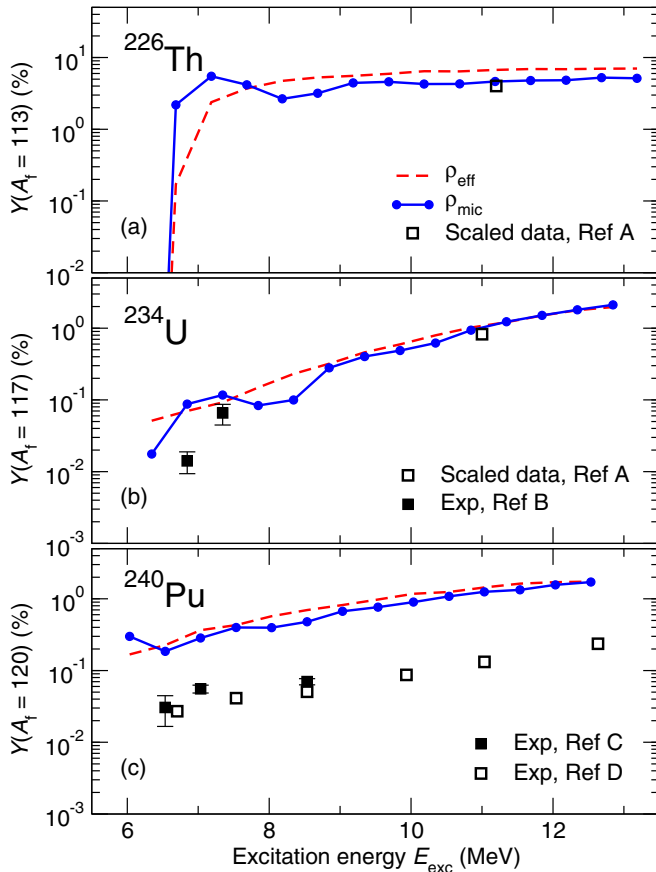
FIG. 11. Symmetric mass yields versus excitation energy for (a) ^{226}Th, (b) ^{234}U, and (c) ^{240}Pu. The calculated yields are obtained with ρ_{mic} (blue circles) or ρ_{eff} as in Ref. [2] (dashed red curve). The squares show various experimental data from Refs. [22] (A), [21] (B), [21] (C), and [23] (D); the charge yields from Ref. [22] have been multiplied by Z/A.

is essentially determined by the excitation energy above the macroscopic liquid-drop energy, which will favor symmetric shapes at all elongations and lead to a wide mass distribution centered at symmetry.

The calculated yields correspond to first-chance fission. At excitation energies above ≈ 11 MeV the system is above the second-chance fission threshold, with an increasing relative probability of multichance fission as the energy is further increased. Therefore the results in Fig. 10 cannot be compared directly to experiments with, e.g., high-energy neutrons impinging on ^{235}U.

Figure 11 shows calculated and experimental mass yields at symmetry as a function of excitation energy for ^{226}Th, ^{234}U, and ^{240}Pu. (To compare with the GSI data [22], the measured charge yield at symmetry $Y(Z_{\mathrm{f}})$ has been multiplied Z/A, where Z and A are the charge and mass numbers of the compound nucleus.) The general increase of the symmetric yield with increasing excitation energy is well reproduced by the calculations. However, for ^{240}Pu, the calculations overpredict the symmetric yield by about a factor of 10.

In Fig. 11, the results from using the microscopic level densities are compared with calculations using the recipe of
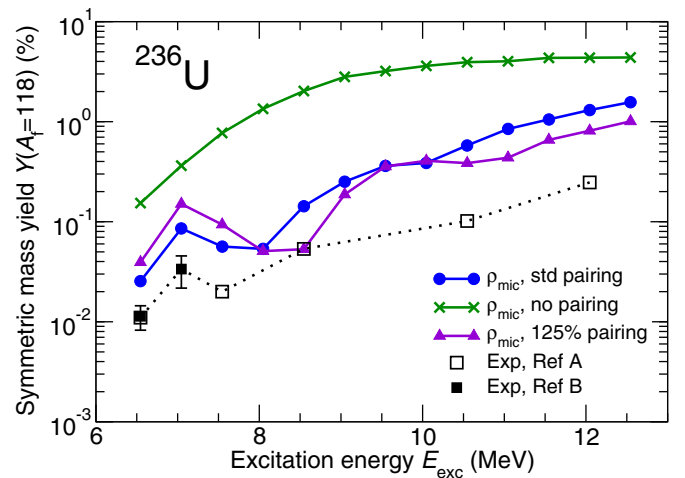

FIG. 12. Mass yields (logarithmic scale) at symmetry for ^{236}U shown versus excitation energy. The calculated results (blue circles) are compared with experimental data A (open squares) from Ref. [24] and B (filled squares) from Ref. [21]. Results of two additional calculations are also shown, one where the level densities are obtained without pairing (green crosses) and one where the pairing strength is increased by 25% (triangles). The potential-energy surface used in the three calculations is the same, consistent with standard pairing.

Ref. [2] in which the microscopic contributions to the potential energy are attenuated by means of an adjusted suppression function. The latter method yields a monotonic increase of the symmetric yield with increasing energy, while the use of microscopic level densities leads to a more complicated structure showing bumps in the yield.

To examine more closely this non-monotonic behavior, Fig. 12 displays results for the nucleus ^{236}U obtained with different strengths of the pairing interaction entering into the microscopic level densities. With the standard parameters, the yield at symmetry has a local maximum at $E_{\mathrm{exc}} = 7$ MeV, followed by a local minimum at 8 MeV. This bump is followed by a second bump ending with an inflection at around 10 MeV. The experimental data show a qualitatively similar behavior, in particular a local maximum at $E_{\mathrm{exc}} = 7$ MeV, although the calculated yields generally exceed the data by a factor of 3–10.

The nonmonotonic behavior of the symmetric yield seen in Figs. 11 and 12 has its origin in the structure of the microscopic level density related to pairing. To highlight the effect of pairing, two additional calculations of the symmetric fission yield of ^{236}U were performed based on different microscopic level densities: one where the pairing is increased to produce a 25% larger mean pairing-gap and another without any pairing. In order to make the interpretation of the results more straightforward, the potential energy (obtained with standard pairing strength) was kept the same. For any given excitation energy E_{exc}, the local excitation energy at each shape is then the same in all three calculations.

Figure 12 shows that the symmetric yield is highly sensitive to the pairing properties of the level density. As the pairing is increased the two bumps in yield as a function of excitation energy are more pronounced. Without pairing the symmetric
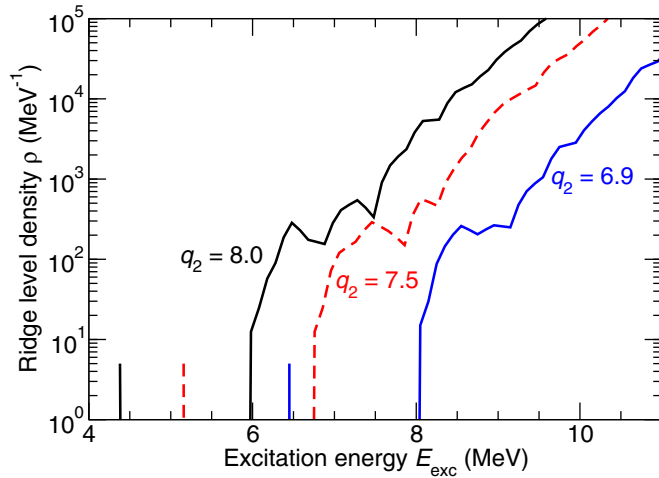
FIG. 13. Level densities at the first three accessible points along the ridge separating the asymmetric and symmetric valleys.

yield is generally larger and increases smoothly with excitation energy. These features resemble features of the level density: without pairing the level density is a smoothly increasing function from the lowest energy state, while pairing creates a gap in the level density and introduces more structure. When the pairing-free level density is used, the absence of a gap produces a larger level density at a given local excitation energy. The increase is larger at shapes with positive shell-correction energies, as the single-particle level density and the pairing gap are both larger.

As discussed and illustrated in Sec. IV A, when fissioning at low energy the nucleus starts out being asymmetric and in order to acquire symmetric shapes the ridge must be surmounted (see Fig. 4). The probability of crossing the ridge depends strongly on the level density for shapes around the ridge.

Figure 13 shows the level density as a function of the excitation energy E_{exc} for three shapes along the ridge. The shell energy E_{sh} for these deformations is positive, yielding a dense single-particle spectrum and a large pairing gap. The level densities have bumps characteristic of the quasiparticle structure of low-lying excitations: The ground state has no quasiparticle excitations; the two-quasiparticle states begin to appear above a gap caused by the breaking of a pair, and after yet another pair-breaking the four-quasiparticle states follow. This structure creates the bumps in the level density (cf. Ref. [25]). It should be recognized that the ridge may be surmounted not just at a single crossing point in the 5D shape space, but at many different locations along the ridge line, which implies an entire distribution of effective ridge energies. At each of these shapes, the level density will qualitatively display the structure shown by the three examples on Fig. 13. Tentatively, one may ascribe the local maximum in the symmetric yield in Fig. 12 to the onset of two-quasiparticle states and the bump around 9 MeV to the onset of four-quasiparticle states. A stronger pairing produces a larger gap and, consequently, shifts this structure to correspondingly higher excitation energies.

V. CONCLUSIONS AND OUTLOOK

We have refined the Metropolis-walk approximation to the Brownian-motion treatment of fission dynamics [1] by employing microscopic local level densities obtained by the recently developed combinatorial method [6]. Because the single-particle levels used are the same as those employed for the macroscopic-microscopic calculation of the potential-energy surfaces, the approach is consistent and no new parameters need be introduced. Moreover, the combinatorial procedure provides access to the level density for a fixed value of angular momentum.

In order to reduce the considerable computing effort required for calculating the level density up to sufficiently high excitations, we employ an analytical extension above ≈ 6 MeV where the combinatorial level density has become smooth. This procedure uses a damped backshift of the excitation energy based on the local pairing and shell energies. In this manner, we have obtained the local level density $\rho(N,Z,E,I;\boldsymbol{\chi})$ for over five million shapes of several nuclei in the uranium region and for angular momenta up to $I = 9$.

Using these parameter-free microscopic level densities with the Metropolis-walk method, we calculate fission fragment charge distributions for ^{226}Th, ^{234,236}U, and ^{240}Pu. The agreement with experimental data was on par with or better than the yields obtained previously with a phenomenological level-density parametrization [2]. The angular-momentum dependence of the fission yields was found to be relatively small and decreasing with increasing excitation energy.

Because the microscopic level densities automatically contain the diminishing effects of pairing correlations and shell structure, the present refined model makes it possible to make more detailed predictions for the energy dependence of the fission yields. The gradual transition from asymmetric to symmetric fission and the detailed energy dependence of the symmetric yield were studied.

Particularly interesting is the finding that the symmetric fragment yield is not monotonically increasing with excitation energy. This perhaps counterintuitive effect appears to be a result of the large pairing correlations for shapes with positive shell-correction energies separating the asymmetric-fission path from symmetric shapes. It is in this connection intriguing that a recent experiment has reported a nonmonotonic energy dependence of the asymmetric peak shape in the fragment mass yields for fission of ^{240}Pu [26]. We plan to investigate these phenomena in more detail.

The present refined model provides a consistent and computationally manageable theoretical framework for studying large-scale collective motion of warm nuclear systems far from equilibrium and, in particular, it provides a unique tool for calculating energy-dependent fission fragment mass distributions. The present work extends the use of microscopic level densities from nuclei in shape equilibrium to arbitrary shapes, and our present studies have revealed the intriguing possibility that the pairing interaction in shapes far from equilibrium may manifest itself in a measurable manner through the energy dependence of the fission yields.

APPENDIX: EFFECTIVE POTENTIAL

In the earlier approximative treatment [2], the gradual attenuation of the microscopic structure effects was taken into account by replacing the true potential U, Eq. (12),

$$U(\boldsymbol{\chi}) = U_{\text{macro}}(\boldsymbol{\chi}) + U_{\text{micro}}(\boldsymbol{\chi})$$
$$= U_{\text{macro}}(\boldsymbol{\chi}) + E_{\text{sh}}(\boldsymbol{\chi}) + E_{\text{pc}}(\boldsymbol{\chi}) - \tilde{E}_{\text{pc}}(\boldsymbol{\chi}), \quad \text{(A1)}$$

with an energy-dependent effective potential U_E,

$$U_E(\boldsymbol{\chi}) = U_{\text{macro}}(\boldsymbol{\chi}) + \mathcal{S}(E_{\text{intr}}(\boldsymbol{\chi}))[E_{\text{sh}}(\boldsymbol{\chi})$$
$$+ E_{\text{pc}}(\boldsymbol{\chi}) - \tilde{E}_{\text{pc}}(\boldsymbol{\chi})], \quad \text{(A2)}$$

where $E_{\text{intr}}(\boldsymbol{\chi}) = E - U(\boldsymbol{\chi})$ is the local excitation energy and $\mathcal{S}(E_{\text{intr}})$ is a phenomenological suppression function that decreases monotonically from $\mathcal{S}(0) = 1$ towards zero as E_{intr}

is increased. Thus the effective potential U_E equals the true potential U for $E_{\text{intr}} = 0$, whereas it approaches U_{macro} as E_{intr} grows large.

Such a simple and intuitively appealing description is generally not possible in the present treatment based on microscopic level densities. However, a correspondence exists above the matching energy E_{m} where the level density is given an analytical form. In that energy regime, one may define the effective potential as

$$\tilde{U}(\boldsymbol{\chi}) = U(\boldsymbol{\chi}) - [\tilde{E}_{\text{intr}}(\boldsymbol{\chi}) - E_{\text{intr}}(\boldsymbol{\chi})]$$
$$= U_{\text{macro}}(\boldsymbol{\chi}) - \tilde{E}_{\text{pc}}(\boldsymbol{\chi})$$
$$+ e^{-E_{\text{intr}}(\boldsymbol{\chi})/E_{\text{d,sh}}} E_{\text{sh}}(\boldsymbol{\chi}) + e^{-E_{\text{intr}}(\boldsymbol{\chi})/E_{\text{d,pc}}} E_{\text{pc}}(\boldsymbol{\chi}),$$
$$\text{(A3)}$$

where the expression (7) for $\tilde{E}_{\text{intr}}$ has been used. Thus the single suppression function $\mathcal{S}(E_{\text{intr}})$ used in Ref. [2], which acted on the combined shell and pairing corrections, has been replaced by two separate suppression functions,

$$\mathcal{S}_{\text{sh}}(E_{\text{intr}}) = e^{-E_{\text{intr}}(\boldsymbol{\chi})/E_{\text{d,sh}}}, \quad \text{(A4)}$$

$$\mathcal{S}_{\text{pc}}(E_{\text{intr}}) = e^{-E_{\text{intr}}(\boldsymbol{\chi})/E_{\text{d,pc}}}, \quad \text{(A5)}$$

acting on the shell correction and pairing condensation, respectively.

[1] J. Randrup and P. Möller, Phys. Rev. Lett. **106**, 132503 (2011).

[2] J. Randrup and P. Möller, Phys. Rev. C **88**, 064606 (2013).

[3] P. Möller, A. J. Sierk, T. Ichikawa, A. Iwamoto, R. Bengtsson, H. Uhrenholt, and S. Åberg, Phys. Rev. C **79**, 064304 (2009).

[4] P. Möller, J. Randrup, and A. J. Sierk, Phys. Rev. C **85**, 024306 (2012).

[5] P. Möller and J. Randrup, Phys. Rev. C **91**, 044316 (2015).

[6] H. Uhrenholt, S. Åberg, A. Dobrowolski, Th. Døssing, T. Ichikawa, and P. Möller, Nucl. Phys. A **913**, 127 (2013).

[7] J. Randrup and R. Vogt, Phys. Rev. C **80**, 024601 (2009).

[8] O. Litaize and O. Serot, Phys. Rev. C **82**, 054616 (2010).

[9] B. Becker, P. Talou, T. Kawano, Y. Danon, and I. Stetcu, Phys. Rev. C **87**, 014617 (2013).

[10] R. Bengtsson and S. Åberg, Phys. Lett. B **172**, 277 (1986).

[11] J. R. Huizenga and L. G. Moretto, Annu. Rev. Nucl. Sci. **22**, 427 (1972).

[12] A. Bohr and B. R. Mottelson, *Nuclear Structure II* (Benjamin, Reading, MA, 1974).

[13] A. V. Ignatyuk, K. K. Istekov, and G. N. Smirenkin, Yad. Fiz. **29**, 875 (1979) [Sov. J. Nucl. Phys. **29**, 450 (1979)].

[14] T. Ericsson, Adv. Phys. **9**, 425 (1960).

[15] N. Metropolis, A. W. Rosenbluth, M. N. Rosenbluth, A. H. Teller, and E. Teller, J. Chem. Phys. **21**, 1087 (1953).

[16] J. R. Nix, Nucl. Phys. A **130**, 241 (1969).

[17] H. Olofsson, R. Bengtsson, and P. Möller, Nucl. Phys. A **784**, 104 (2007).

[18] J. Randrup, P. Möller, and A. J. Sierk, Phys. Rev. C **84**, 034613 (2011).

[19] T. Ichikawa, I. Iwamoto, P. Möller, and A. J. Sierk, Phys. Rev. C **86**, 024610 (2012).

[20] S. Åberg, B. G. Carlsson, Th. Døssing, and P. Möller, Nucl. Phys. A **941**, 97 (2015).

[21] M. B. Chadwick *et al.*, Nucl. Data Sheets **112**, 2887 (2011).

[22] K.-H. Schmidt, S. Steinhäuser, C. Bäckstiegel, A. Grewe, A. Heinz, A. R. Junghans, J. Benlliure, H.-G. Clerc, M. de Jong, J. Müller, M. Pfützner, and B. Voss, Nucl. Phys. A **665**, 221 (2000).

[23] J. E. Gindler, L. E. Glendenin, D. J. Henderson, and J. W. Meadows, Phys. Rev. C **27**, 2058 (1983).

[24] L. E. Glendenin, J. E. Gindler, D. J. Henderson, and J. W. Meadows, Phys. Rev. C **24**, 2600 (1981).

[25] T. Døssing, T. L. Khoo, T. Lauritsen, I. Ahmad, D. Blumenthal, M. P. Carpenter, B. Crowell, D. Gassmann, R. G. Henry, R. V. F. Janssens, and D. Nisius, Phys. Rev. Lett. **75**, 1276 (1995).

[26] M. E. Gooden *et al.*, Nucl. Data Sheets **131**, 319 (2016).